Multimechanism quantum anomalous Hall and Chern number tunable states in germanene (silicene, stanene)/MBi$_2$Te$_4$ heterostructures

Zhe Li,[1,*] Jiatong Zhang,[2] Xiyu Hong,[2] Xiao Feng,[2,3,4,5] and Ke He[2,3,4,5]
[1]*Beijing National Research Center for Condensed Matter Physics, and Institute of Physics, Chinese Academy of Sciences, Beijing 100190, China*
[2]*State Key Laboratory of Low Dimensional Quantum Physics, Department of Physics, Tsinghua University, Beijing 100084, China*
[3]*Beijing Academy of Quantum Information Sciences, Beijing 100193, China*
[4]*Frontier Science Center for Quantum Information, Beijing 100084, China*
[5]*Hefei National Laboratory, Hefei 230088, China*

(Received 4 March 2024; revised 16 May 2024; accepted 31 May 2024; published 17 June 2024)

By constructing germanene (silicene, stanene)/MBi$_2$Te$_4$ ($M = 3d$-transition elements) heterostructures, we discovered and designed multimechanism quantum-anomalous-Hall (QAH) systems, including Γ-based QAH, K-K'-connected QAH, and valley-polarized K- or K'-based QAH states via first-principle computations. The unique systems possess a global gap and tunable Chern number. The coexisting conventional Γ-based QAH state of MBi$_2$Te$_4$ and valley-polarized $K(K')$-based QAH state of germanene (silicene, stanene), with opposite chirality, can interact with each other. Adjusting magnetic configurations of MBi$_2$Te$_4$-layers not only switch on (off) the QAH conductance, but also modulate Chern numbers exactly. For example, the germanene/bilayer-NiBi$_2$Te$_4$ possesses the Chern number $C = +1$ in ferromagnetic couplings and $C = +2$ in antiferromagnetic couplings. The novel multimechanism QAH insulators, which are achievable in experiments, provide a new approach to spintronics and valleytronics based on topological states of matter.

DOI: 10.1103/PhysRevB.109.235132

Recently, the design of magnetic topological materials towards various requirements of quantum anomalous Hall (QAH) effect attracted numerous attention [1–32]. Initially put forward in certain periodically magnetic-field-assisted graphene [1] and fabricated in magnetic-doped topological insulators [3], QAH states inspired new research hotspots owing to its dissipationless edge-conductance, with no need for strong external field and further investigations for Majorana fermions, axions, topological magnetoelectric fields [15,18,24,25], and so on. Noticeably, the MnBi$_2$Te$_4$-family of materials is a representatively intrinsic van der Waals (vdW) stacked topological magnet [13–22] that has potential for both high-temperature QAH [17,19] and Chern-number-tunable character after being neighbored with monolayer Bi [30] in which p electrons of MnBi$_2$Te$_4$ or Bi hybridize with d electrons of Mn to create QAH conductance. Another route is to build QAH magnets derived from d-d electron correlations, like Pd(Pt)Br(I)$_3$, MnBr$_3$, LiFeSe, NiAs(Bi)O$_3$, PdSbO$_3$ [26–29,32], and so on. All these systems generate QAH edge-states originated from only one certain mechanism.

Distinct from the mechanisms mentioned above, the third mechanism to motivate the QAH effect depends on the band topology of $K(K')$ valleys, which was initially proposed in basic models of silicene [33,34]. Researchers paid great efforts to finding perfect magnetic substrates to these group-IV-element monolayers [35–40], and predicted QAH effects in some candidates [35–39]. However, up to now the predictions and accomplishments of flexibly tuning Chern and valley-polarized-Chern numbers via real materials are still lacking. Furthermore, combining and coupling multimechanisms of QAH in one system triggered by even one magnetic origin is still a mystery.

In this work, we systematically discover and design multimechanism quantum-anomalous-Hall states (mQAH) via constructing germanene (silicene, stanene)/MBi$_2$Te$_4$ vdW heterostructures. Among all these cases, germanene behaves the best due to its large global gaps and large Γ (K, K')-based gaps. Monolayer germanene, which is neighbored by MnBi$_2$Te$_4$ and NiBi$_2$Te$_4$, can generate both K-K'-connected QAH and valley-polarized QAH (vpQAH) states at K or K' valleys, of which the total Chern number and valley-polarized-Chern number are $C = +2$ and $C_v = -1$, respectively, and the mass term is motivated by $3d$ orbitals of Mn or Ni atoms. Moreover, by neighboring thicker layers of Mn(Ni)Bi$_2$Te$_4$, the mQAH state combining Γ-based QAH and $K(K')$-based vpQAH states forms, both of them triggered only by Mn(Ni)-$3d$ orbitals and sharing the opposite chirality. NiBi$_2$Te$_4$ behaves better than MnBi$_2$Te$_4$ with larger gaps [25], which is more appealing for experimental surveys. Remarkably, stacking-order shift is an experimentally available method for tuning mass terms, intrinsic, and extrinsic Rashba terms [33,34] in vpQAH characters of germanene. Via stacking-order shift, we obtained phase-diagram mappings

*Contact author: lizhe21@iphy.ac.cn

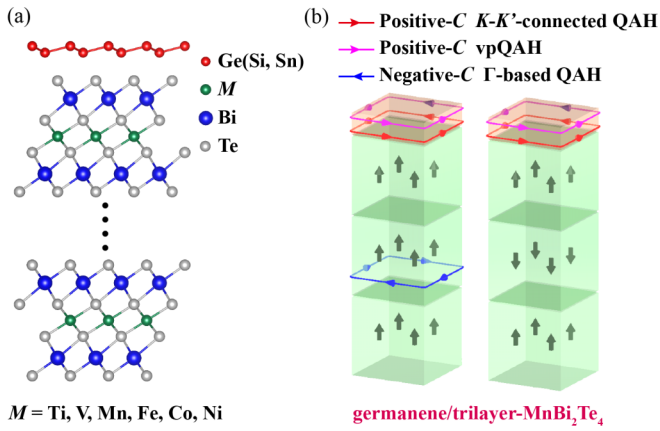

FIG. 1. Lattice structures and illustrations of mQAH state in germanene (silicene, stanene)/MBi$_2$Te$_4$. (a) Side view of monolayer-germanene (silicene, stanene)/few-layer-MBi$_2$Te$_4$, in which red, green, blue, and light gray balls denote Ge (Si, Sn), M, Bi, and Te atoms, respectively. (b) Illustrations of mQAH state in germanene/trilayer-MnBi$_2$Te$_4$ under FM and AFM configurations. Light-brown and light-green blocks are layers of germanene and MnBi$_2$Te$_4$. The circular arrows colored with red, pink, and blue are positive-chiralized K-K'-connected QAH, positive-chiralized vpQAH, and negative-chiralized Γ-based QAH conductances, respectively.

corresponding to different Chern-insulating phases, providing a paradigmatic case for switchable and tunable Chern and valley-Chern numbers in real materials.

Crystallized by a low-buckled, hexagonal structure, monolayer germanene (silicene, stanene) shares similar lattice structures with MBi$_2$Te$_4$ in which we compare the in-plane lattice mismatch in the Supplemental Material [41] (see also Refs. [13,21,22,24,25,33,42–53] and references therein) as Table S1. Clearly, both germanene and stanene can approximately match MBi$_2$Te$_4$ by the ratio of 1:1 within $\pm 10\%$ of the lattice mismatch, while in the case of silicene, only NiBi$_2$Te$_4$ falls in this range. The absolute value of the in-plane lattice constants of these monolayer compounds are listed in Table S2. For MBi$_2$Te$_4$, we select M as Ti, V, Mn, Fe, Co, and Ni due to their mechanically stable structures and large global gaps in which the first are verified by density functional perturbation theory in Fig. S1 and the second are confirmed by band structures (Fig. S2). Lattice mismatch brings biaxial strains into both germanene (silicene, stanene) and MBi$_2$Te$_4$ without causing structural instabilities (see Figs. S3 to S6). Moreover, opting for MBi$_2$Se$_4$ and MSb$_2$Te$_4$ reaches less lattice mismatch, but contains a rather severe requirement to achieve large-gapped QAH states (Fig. S7), so we mainly focus on that of MBi$_2$Te$_4$ below.

Depicted in Fig. 1(a), germanene (silicene, stanene) stacks as the order $ABCABC$ along the (111) directions, similar to that of multilayer MBi$_2$Te$_4$ itself. In this single heterostructure, MBi$_2$Te$_4$ itself contains a conventional Γ-based QAH state under a multilayer regime. In the meantime, MBi$_2$Te$_4$ also breaks time-reversal symmetry (TRS), brings mass terms in germanene (silicene, stanene) to create $K(K')$-based, both K-K'-connected QAH and vpQAH states in the latter. We call this phenomenon the multimechanism QAH state (abbreviated as mQAH) in which there is only one origin: the M element in MBi$_2$Te$_4$ triggers two or more kinds of different mechanisms of QAH states that coexist in the same system and even interact with each other. This concept unfolds a new field of the QAH state and magnetic-topology with possibly more abundant phase diagrams, compared to the previous works that mainly contained single-mechanism QAH states [3–7,13–30,33–39].

Choosing germanene/trilayer(TL)-MnBi$_2$Te$_4$ as an example, we draw illustrations of mQAH behaviors under different magnetic configurations in Fig. 1(b). The ferromagnetic (FM) state MnBi$_2$Te$_4$ is necessary to generate the Γ-based QAH state in itself. If the interlayer couplings of MnBi$_2$Te$_4$ recover to the antiferromagnetic (AFM) state, the Γ-based QAH state vanishes, meanwhile the K-K'-connected QAH and vpQAH states still remain, protected by the most proximate MnBi$_2$Te$_4$-layer. Hereafter the computational results below will describe these behaviors in detail.

Figure 2(a) shows the orbital project-band structure of germanene/monolayer-MnBi$_2$Te$_4$. Fortunately, the gaps at the Γ-point and $K(K')$ valley are ideally aligned to the same energy scope located at the Fermi level (see Table S4). The contributions from Ge-p_z orbitals mainly occupy valleys around the K and K' points, similar to that of free-standing stanene [54,55]. However, the gaps around the K valleys are greatly shrunken compared to those around the K' valleys in which the degeneracy is lifted by the breakage of inversion-symmetry. The asymmetry between K and K' is more obvious in the local density-of-state (LDOS) distribution along the [100] boundary [Fig. 2(b)]. For the K valley, two positive-chiralized edge states appear between conductance and the valence band, meanwhile no edge state exists within the gap at the K' valley. Figure 2(c) exactly confirms the $C = +2$ character around the K valley, with the gap around 2.5 meV. To verify its valley-polarized character, Berry curvature distributions are computed in Fig. 2(d). Obviously, Berry curvatures around K and K' valleys are totally different, giving integration results as $+1.5$ and $+0.5$, respectively. Therefore, the total Chern number is $C = +2$, while its valley-polarized nature is affirmed as $C_v = C_K - C_K = -1$. Here, a K-K'-connected QAH edge state contributing no valley-polarized nature connects the valence band at the K' valley and conductance band at the K valley, exhibited in Fig. S12. MnBi$_2$Te$_4$ behaves as a multifunctional substrate via breaking both TRS and inversion symmetry, and containing a strong spin-orbital coupling (SOC) effect, which leads to considerable intrinsic and extrinsic Rashba-SOC terms acting on the germanenes low-buckled structure and global-gapped vpQAH state that was proposed with basic models [33,34].

Monolayer MnBi$_2$Te$_4$ itself has no QAH conductance due to its strong intralayer-quantum confinement. Considering thicker-layer conditions, and selecting FM-state TL-MnBi$_2$Te$_4$ as an example, we successfully motivate the Γ-based QAH state within TL-MnBi$_2$Te$_4$ while maintaining vpQAH states in germanene [Figs. 2(e) to 2(h)]. The freely relaxed structure has band-gap-misplacement between the $K(K')$ and Γ point, destroying the global gap. To obtain gap alignment, -1.0% of biaxial strain is implemented (see the analysis in Table S4 and Fig. S8). Amazingly, the single

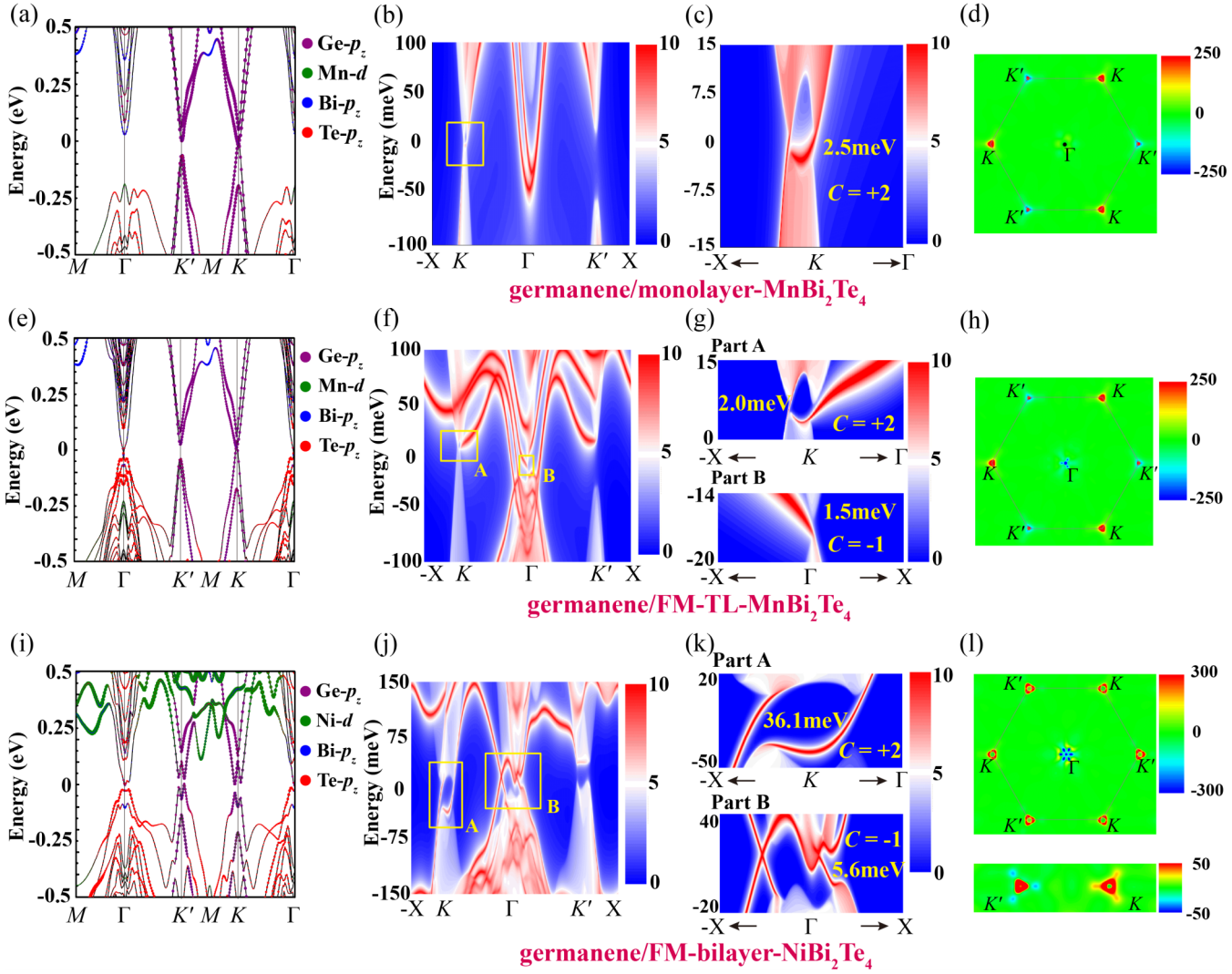

FIG. 2. Band structures, LDOS, and Berry curvatures of germanene/Mn(Ni)Bi_2Te_4. (a) Orbital project-band structures of germanene/monolayer-$MnBi_2Te_4$. Purple, olive, blue, and red bubbles stand for Ge-p_z, Mn-d, Bi-p_z and Te-p_z contributions, respectively. (b) LDOS distribution of germanene/monolayer-$MnBi_2Te_4$ cut along [100] boundary. (c) Zoom-in LDOS distribution around the gap at the K valley. (d) Berry curvatures of germanene/monolayer-$MnBi_2Te_4$ distributing along the two-dimensional Brillouin zone. (e)–(h) are similar with (a)–(d), but in the case of FM state germanene/TL-$MnBi_2Te_4$. (i)–(l) are also similar with (a)–(d), but under FM state germanene/bilayer-$NiBi_2Te_4$. In (i) olive bubbles denote Ni-d contributions.

magnetic-moment origin of Mn element breaking TRS produces the opposite chirality between the Γ-based QAH state in TL-$MnBi_2Te_4$ and $K(K')$-based QAH state in germanene, resulting in a compensated Chern number $C = +1$. No global gap exists, but regional gaps open both around the Γ point and K valley, manifesting QAH edge states clearly within each gap [Fig. 2(g)]. A negative Berry curvature contributing the integration of -1 emerges at the Γ point relating to the QAH state in TL-$MnBi_2Te_4$ [Fig. 2(h)], with the valley-polarized Berry curvature being retained at the $K(K')$ valleys, authenticating its mQAH character. Notably, when TL-$MnBi_2Te_4$ recovers AFM configuration, $K(K')$-based QAH states survive but the Γ-based QAH state disappears, with the total Chern number recovering to $+2$, evolving the Chern-tunable capability [see Figs. S13(i) to S13(k)]. This behavior indicates that $K(K')$-based QAH states in germanene only depend on the most neighboring $MnBi_2Te_4$ layer. Due to weak interlayer coupling between $MnBi_2Te_4$ layers [13,21], a moderate strength of the out-of-plane magnetic field can modulate $C = +2$ to $C = +1$, which is easily manipulated under experimental conditions.

$NiBi_2Te_4$ performs much better than $MnBi_2Te_4$ owing to its stronger ability to create mass terms both from Coulomb and kinetic interactions [25]. Figures 2(i) to 2(l) depict the results of germanene/bilayer-$NiBi_2Te_4$ under the FM coupling and biaxial strain of $+1.3\%$. Evidently, the global gap opens in the whole Brillouin zone (BZ), with the nontrivial gap at the K valley up to 36.1 meV, manifesting it as the potential for high-temperature QAH. Bilayer-$NiBi_2Te_4$ engenders not only moderate gaps at the Γ point (5.6 meV), but also a sizable mass term at the $K(K')$ valleys, comprising the large-gapped mQAH state. Similar to germanene/TL-$MnBi_2Te_4$, it generates the mQAH state with $C = +1$ under FM coupling and $C = +2$ when bilayer $NiBi_2Te_4$ regains the AFM ground state. It's an excellent candidate for investigating $K(K')$-based

TABLE I. Chern-insulating and tunable behaviors of germanene/MBi$_2$Te$_4$. Red digits are denoted as Chern-number-tunable conditions, while "Metallic" means the system has no gap whether at Γ point or at $K(K')$ valley. All the cases are derived under the out-of-plane magnetic-moment condition.

MBi$_2$Te$_4$	Magnetism	Monolayer	Bilayer	Trilayer
TiBi$_2$Te$_4$	FM	0	0	Metallic
	AFM	–	0	Metallic
VBi$_2$Te$_4$	FM	0	0	Metallic
	AFM	–	0	Metallic
MnBi$_2$Te$_4$	FM	+2	+2	+1
	AFM	–	+2	+2
FeBi$_2$Te$_4$	FM	+2	+2	Metallic
	AFM	–	+2	Metallic
CoBi$_2$Te$_4$	FM	+2	+2	Metallic
	AFM	–	+2	Metallic
NiBi$_2$Te$_4$	FM	+2	+1	Metallic
	AFM	–	+2	Metallic

vpQAH and Γ-based QAH states, but hard for Chern-tunable applications due to its stronger interlayer magnetic couplings [13,21].

We systematically investigate germanene/MBi$_2$Te$_4$ when M = Ti, V, Mn, Fe, Co and Ni by setting out-of-plane magnetism first. Among all of them, Ti and V have no ability to induce QAH conductance limited by their weak Coulomb and kinetic interactions [25]. Mn holds enough ability to motivate vpQAH states in germanene from monolayer to TL, but possesses the mQAH state only at the FM, TL regime. Fe and Co behave similarly to that of Mn, but their potential mQAH states are blocked by band overlapping in TL (Figs. S16 and S17). Chern numbers of the only two candidates of mQAH and Chern-number-tunable systems (germanene/TL-MnBi$_2$Te$_4$ and germanene/bilayer-NiBi$_2$Te$_4$) are listed in Table I with red and the LDOS results of all the discussed heterostructures above are depicted in Fig. 2 and Figs. S13 to S17, verifying Chern numbers in every condition listed in Table I. By ruling out the other four candidates, we list magnetic crystalline anisotropy energies of germanene/TL-MnBi$_2$Te$_4$ and germanene/bilayer-NiBi$_2$Te$_4$ in Table S6, confirming their ground state lies in out-of-plane magnetism.

It's worth mentioning that moderate biaxial strains cause no influence on the topological features except the case that is located very near to the phase transition point (FM state germanene/TL-MnBi$_2$Te$_4$) shown in Figs. S9 and S10. Furthermore, increasing the values of Hubbard U also fails to induce topological phase transitions with only the local band gap decreasing, which is exhibited in Fig. S11. These outcomes verify the robustness of these novel magnetic topological characters in most cases.

In view of the vdW stacking nature of germanene and MBi$_2$Te$_4$, conveniently using stacking-order shift is an exercisable way to experimentally and continuously manipulate the interplay between germanene and MBi$_2$Te$_4$. Hereinafter, we focus on Chern-number-tunable phase transitions, global, or regional gap-modulating outcomes relying on stacking-order shifts.

Figure 3 displays and analyzes stacking-order-induced phase mappings of germanene/monolayer-MnBi$_2$Te$_4$, FM state germanene/TL-MnBi$_2$Te$_4$, and FM state germanene/bilayer-NiBi$_2$Te$_4$ that we discussed in Fig. 2. For all the three cases, Chern numbers can be step-likely and flexibly modulated with different stacking orders. Considering the case of germanene/monolayer-MnBi$_2$Te$_4$ displayed in Figs. 3(a)–3(c) in which Chern numbers, formation energies and the gap at the K valley distributing along the in-plane-shift primitive cell are shown as mapping patterns. Figure 3(d) concretely illustrates how the germanene layer shifts on the MBi$_2$Te$_4$ layer, within which the two black arrows noted as **a** and **b** mark the two primitive axes. The original point named as AB corresponds to the normal $ABCABC$ stacking order. After atomical relaxations, different stacking orders mainly fall into two phase categories related to the major region of $C = +2$ [the red zone in Fig. 3(a)] and the minor region of $C = 0$ [the yellow zone in Fig. 3(a)], respectively. These two distinguished phase distributions are directly related to the low and high formation energy regions in Fig. 3(b), corresponding to small (∼2.7 Å) and large (∼3.0 Å) vdW distances, respectively (see Fig. S18). Intuitively, the larger vdW distance and higher formation energy weaken the electronic hybridization between germanene and MnBi$_2$Te$_4$, reducing both the intrinsic, extrinsic Rashba-SOC terms and the mass terms, then eliminating both the K-K'-connected QAH and vpQAH states in germanene. In Fig. 3(c), the gaps around the K valley also fall into two categories in which the smaller one (2 meV ∼ 4 meV) corresponds to the $C = +2$ condition while the larger one (above 40 meV) relates to the topologically trivial property. Although the K-valley gaps are small and not sensitive to stacking-order shift, in most regions the whole system holds BZ-global gaps (see Fig. S18), profitably for experimental investigations and applications.

The condition when germanene is proximate to TL-MnBi$_2$Te$_4$ under FM coupling looks more complicated. Both the Chern number of germanene and TL-MnBi$_2$Te$_4$ can be modulated with stacking-order reformation (see Fig. S19). Figure 3(e) delineates a more abundant Chern-number-distribution mapping, offering a step-likely Chern-tunable method from +2 to −1. Similarly, the lower Chern number (−1 and 0) region is related to white-colored, higher formation energies in Fig. 3(f) in which the Chern number in germanene is zero (see Fig. S19). For the higher-Chern number (+1 and +2) region, the K-valley gaps retain between 2 meV to 5 meV, similar to the monolayer-MnBi$_2$Te$_4$ case. The light-red area of $C = +1$ occupies the most part, affirming that the mQAH state is active under most stacking orders. Regrettably, no BZ-global gap exists totally in the whole shifting plane [Fig. S18(g)]. We select the shifting position (1/2, 1/2) that falls in the center of Fig. 3(e), denoted as Point A, which holds the Chern number as −1, to search for more details. Figure 3(h) exhibits the LDOS of Point A in which no chiral edge states cross through the K- and K'-valley gaps, but a residual negative-chiralized edge state crosses through the gap at Γ point, revealing that the $C = -1$ is rooted in TL-MnBi$_2$Te$_4$ itself.

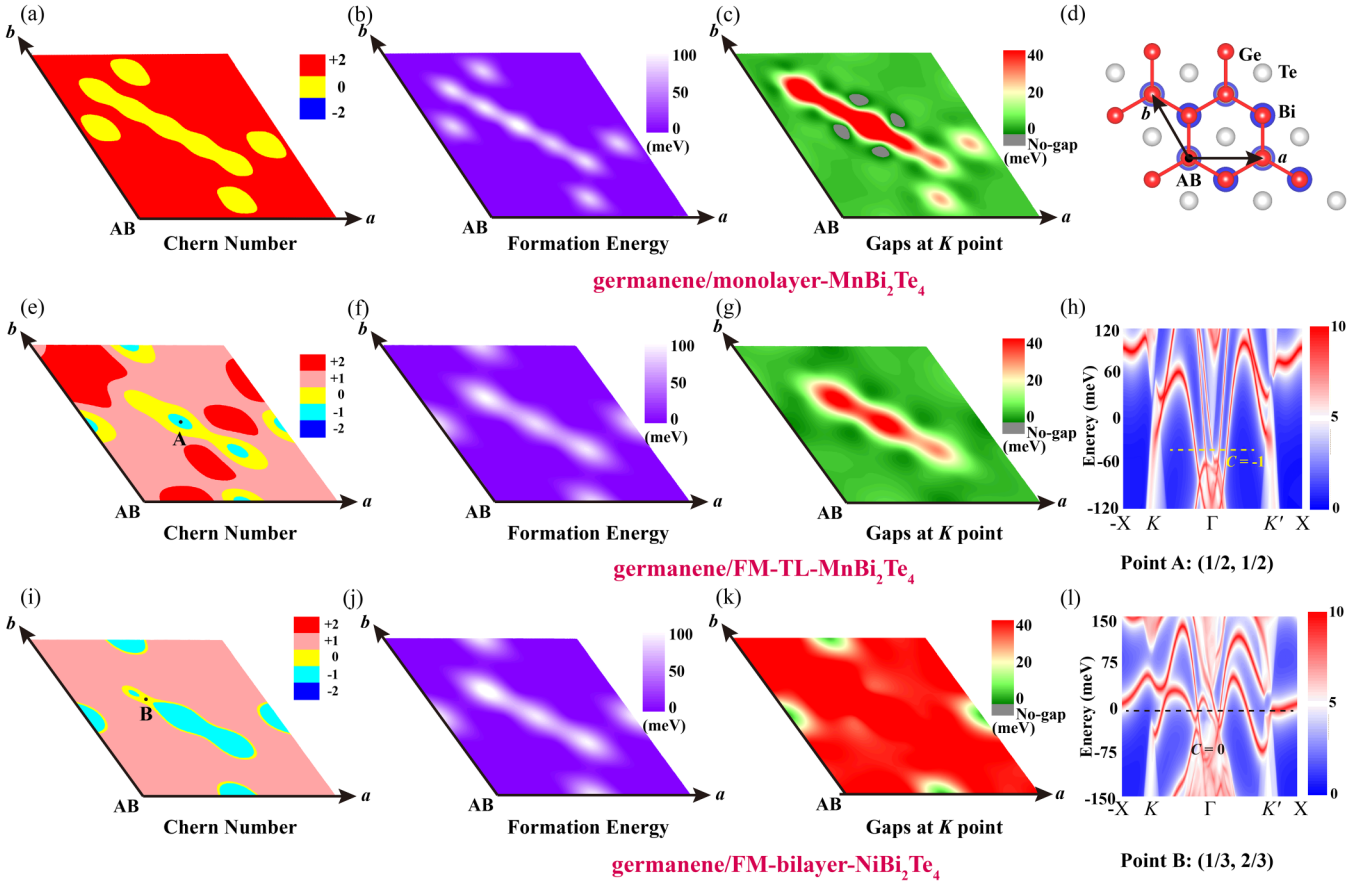

FIG. 3. Stacking-order-shift investigations in germanene/$MnBi_2Te_4$ under monolayer- and TL-$MnBi_2Te_4$ cases. (a)–(c) are the case of germanene/monolayer-$MnBi_2Te_4$. (a) Chern-number distributions along one in-plane shift primitive cell. Red and yellow regions are corresponding to $C = +2$ and $C = 0$ phases, respectively. "*AB*" in the original point means the normal stacking order. (b) The formation energy distributions by setting that under the normal stacking order to zero. From purple to white, the formation energy increases. (c) The gap-distributions of the K' valley. From green to yellow and red, the gap increases. Dark-gray region means no gap. (d) A schematic illustration of stacking-order-shifts between germanene and MBi_2Te_4. Red, light-gray, and blue balls stand for Ge, Te and Bi atoms. Two black arrows are related to primitive axes on in-plane shift. (e)–(g) are similar to (a)–(c), but under the case of FM state germanene/TL-$MnBi_2Te_4$. (h) LDOS pattern along [100] boundary at the Point A (1/2, 1/2) of stacking order noted in (e). (i)–(k) are similar to (a)–(c), but under the case of FM state germanene/bilayer-$NiBi_2Te_4$. (l) LDOS pattern along [100] boundary at the Point B (1/3, 2/3) of stacking order noted in (i).

Moreover, we depict the stacking-order-shift behaviors of FM-state germanene/bilayer-$NiBi_2Te_4$ in Figs. 3(i)–3(l), which shares similar performance with that of germanene/FM-TL-$MnBi_2Te_4$, but possesses a rather more robust Chern-insulating property orginating from bilayer-$NiBi_2Te_4$, excluding the $C = +2$ area absolutely [Fig. 3(i)]. Remarkably, Ni contributes larger mass terms than Mn [25], bringing and retaining larger K-valley gaps even above 30 meV at the largest part of the stacking-order-shift positions [Figs. 3(j) and 3(k)]. Figure 3(l) shows the LDOS pattern in the position (1/3, 2/3) shown in Fig. 3(i) that is labeled as "Point B", in which the "$C = 0$" nature originates from the competitive character of Chern-insulating mechanisms from opposite chirality. Consequently, stacking-order shifts can modulate Chern numbers step-likely and glibly meanwhile persisting with the large-gap characters based on this system.

Owning to the same group element and analogous structure, silicene and stanene are expected to possesses the mQAH state including vpQAH state after neighboring MBi_2Te_4. Figure 4 takes silicene/monolayer-$NiBi_2Te_4$ and stanene/monolayer-$MnBi_2Te_4$ as two instances. We choose +2.0% and +2.6% biaxial strains to align the Γ gap and $K(K')$ gap to a similar energy scope as silicene/monolayer-$NiBi_2Te_4$ and stanene/monolayer-$MnBi_2Te_4$, respectively. Opposite to that of germanene/Mn(Ni)Bi_2Te_4, for silicene/monolayer-$NiBi_2Te_4$ the Chern-insulating phenomenon is located on the gap of the K' valley, not the K valley. Zoom-in LDOS patterns in Fig. 4(b) uncover the details, within which no valley-polarized nontrivial edge-state exists at the K-valley (see Part A), meanwhile one $\Gamma - K'$-connected QAH edge-state emerges and another vpQAH edge-state appears at the K' valley, see Part B in Fig. 4(b). Immediately, we arrive at the conclusion that the total Chern number is $C = +2$ and the valley-polarized Chern number $C_v = +1$. Stacking-order shift will modulate the Chern number as +2, +1, and 0 [Fig. 4(c)] while maintaining the gap at the K' valley to about 15meV $\sim$ 20 meV in most positions [Fig. 4(d)]. Surprisingly, in the small zone around the position (1/3, 2/3), the K'-valley

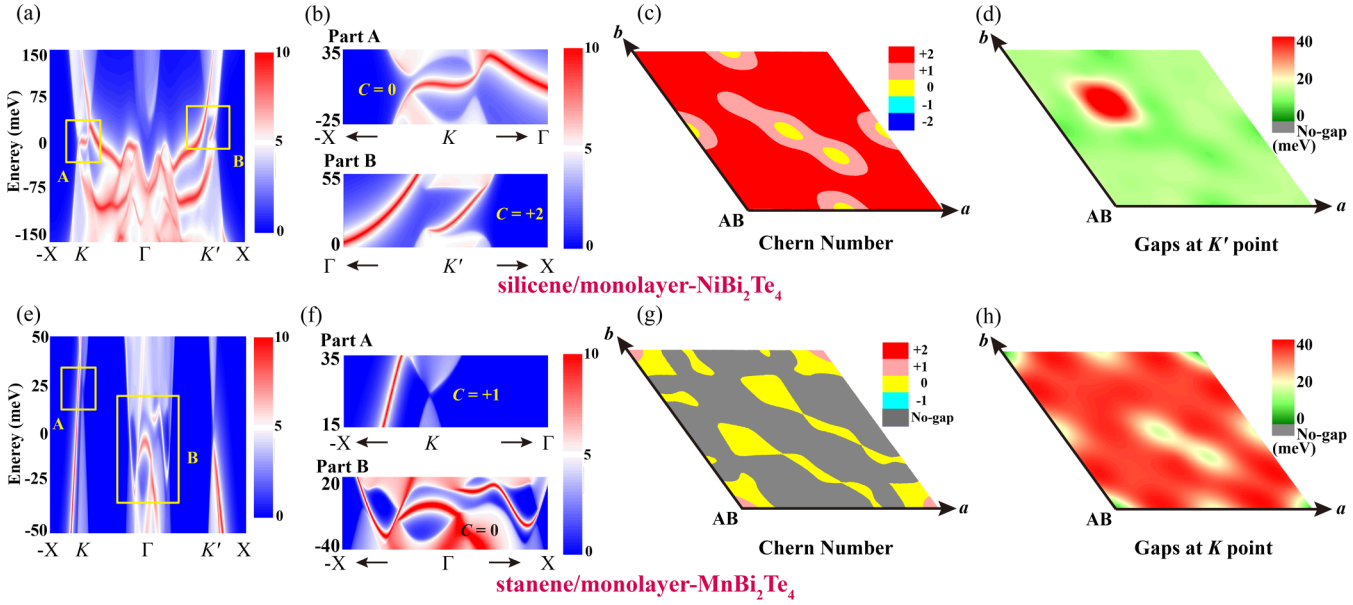

FIG. 4. LDOS of normal stacking-order, stacking-order-shift investigations of Chern numbers and $K(K')$-valley gaps in silicene/monolayer-$NiBi_2Te_4$ and stanene/monolayer-$MnBi_2Te_4$. (a)–(d) are under the case of silicene/monolayer-$NiBi_2Te_4$. (a) LDOS patterns of [100] boundary under normal *ABCABC* stacking order. (b) Two zoom-in LDOS patterns of (a) labeled as part A and part B, respectively, marked with yellow frame in (a). (c) Stacking-shift-dependent Chern-number distributions within in-plane-shift primitive cell. Red, light-red, yellow, cyan, and blue regions are related to $C = +2, +1, 0, -1, -2$, respectively. (d) Chern-insulating K'-valley gap distributions within in-plane-shift primitive cell. From green to yellow and red the gap increases. (e)–(h) are analogous with that of (a)–(d), but correspond to the case of stanene/monolayer-$MnBi_2Te_4$. In (h), we choose nontrivial K-valley gaps, not trivial K'-valley gaps.

gap jumps to above 40 meV with nontrivial Chern-insulating property in the meantime. In this system, not only can the total Chern number, but also the valley-polarized Chern number can be step-likely modulated, shown in Fig. S20. C_v is tuned as $+1$, 0, -1, the function of which is absent in germanene/Mn(Ni)Bi_2Te_4 (see Fig. S18). This is the first predicted valley-polarized Chern-number-tunable material that is experimentally executable via only stacking shifts. Specifically, the valley-polarized Chern number distributions of silicene/monolayer-$NiBi_2Te_4$ show no correspondence with formation energies [Figs. S20(a) and S20(b)]. The global gaps of it vanish in most areas, but exist in several areas smaller than 15 meV [Fig. S20(c)]. The orbital-projected band structures of silicene/monolayer-$NiBi_2Te_4$ and stanene/monolayer-$MnBi_2Te_4$ are displayed in Fig. S21.

Stanene behaves poorly compared to that of germanene and silicene on account of its energy imbalance between the gap at the Γ point and the $K(K')$ valley when choosing $MnBi_2Te_4$ as substrate [40]. For stanene/monolayer-$MnBi_2Te_4$, computational outcomes support a small gap at both the Γ and $K(K')$ points, which is further confirmed in LDOS patterns [Fig. 4(e)]. From the zoomed-in parts in Fig. 4(f), the K valley contributes $C = +1$ and the Γ point supplies $C = 0$, manifesting it as a K-K'-connected QAH insulator with total Chern number $C = +1$. The stacking-order shift now acts as a collapsing force to the Chern-insulating character, destroying its QAH conductance to a trivial feature that is labeled as the yellow zone, and even the metallic phase that is labeled as the dark-gray region in Fig. 4(g). After shifting stanene on the $MnBi_2Te_4$, the gap on the K valley expands above 30 meV for most positions, much higher than the case under the normal stacking order that is only about 3 meV [Fig. 4(h)]. Stanene/$MnBi_2Te_4$ has been successfully experimentally fabricated [40] that was assisted with experiences of growing stanene on Bi_2Te_3 [56], therefore, it's the most probable candidate that achieves K-valley QAH conductance under transport measurements, let alone its barely satisfactory behaviors. Silicene and stanene perform badly for their metallic features as MBi_2Te_4 grows thicker, destroying the potential for accomplishing and measuring mQAH states (see Figs. S22 and S23).

In summary, we discover and carefully burrow the mQAH characters simply via constructing germanene (silicene, stanene)/MBi_2Te_4 heterostructures. Among these systems, germanene is induced as both K-K'-connected QAH and vpQAH states as long as M is selected as Mn, Fe, Co, and Ni. Under FM couplings, germanene/TL-$MnBi_2Te_4$ and germanene/bilayer-$NiBi_2Te_4$ trigger $K(K')$-based QAH and Γ-based QAH states originating from only M elements, producing the opposite chirality between germanene and MBi_2Te_4, which causes a compensated total Chern number. For the condition of bilayer-$NiBi_2Te_4$, the BZ global gap survives in the most stacking orders, and the K-valley gap remains above 30 meV towards high-temperature applications. Stacking-order shifts produce a step-likely Chern-number-tunable method utilizing these heterostructures for which the Chern number is flexibly modulated among $+2$, $+1$, 0, -1 meanwhile retaining the size of the K-valley gap and the Γ gap. For the first time, we not only put forward the concept of the mQAH state, which is predicted in some candidates of germanene/MBi_2Te_4, but also establish

a paradigmatic materials scheme for tunable total-Chern and valley-polarized-Chern insulators, which is greatly beneficial for spintronic (valleytronic) applications.

We thank for X.-Y. Tang and Y. Chen for helpful discussions. This work was supported by the National Natural Science Foundation of China (Grant No. 92065206).

[1] F. D. M. Haldane, Model for a quantum Hall effect without Landau levels: Condensed-matter realization of the "parity anomaly", Phys. Rev. Lett. **61**, 2015 (1988).

[2] R. Yu, W. Zhang, H.-J. Zhang, S.-C. Zhang, X. Dai, and Z. Fang, Quantized anomalous Hall effect in magnetic topological insulators, Science **329**, 61 (2010).

[3] C.-Z. Chang, J. Zhang, X. Feng, J. Shen, Z. Zhang, M. Guo, K. Li, Y. Ou, P. Wei, L.-L. Wang *et al.*, Experimental observation of the quantum anomalous Hall effect in a magnetic topological insulator, Science **340**, 167 (2013).

[4] H. Weng, R. Yu, X. Hu, X. Dai, and Z. Fang, Quantum anomalous Hall effect and related topological electronic states, Adv. Phys. **64**, 227 (2015).

[5] M. Mogi, R. Yoshimi, A. Tsukazaki, K. Yasuda, Y. Kozuka, K. Takahashi, M. Kawasaki, and Y. Tokura, Magnetic modulation doping in topological insulators toward higher-temperature quantum anomalous Hall effect, Appl. Phys. Lett. **107**, 182401 (2015).

[6] Y. Ou, C. Liu, G. Jiang, Y. Feng, D. Zhao, W. Wu, X.-X. Wang, W. Li, C. Song, L.-L. Wang *et al.*, Enhancing the quantum anomalous Hall effect by magnetic codoping in a topological insulator, Adv. Mater. **30**, 1703062 (2018).

[7] Y. Wang, F. Zhang, M. Zeng, H. Sun, Z. Hao, Y. Cai, H. Rong, C. Zhang, C. Liu, X. Ma *et al.*, Intrinsic magnetic topological materials, Front. Phys. **18**, 21304 (2023).

[8] M. Z. Hasan and C. L. Kane, *Colloquium*: topological insulators, Rev. Mod. Phys. **82**, 3045 (2010).

[9] X.-L. Qi and S.-C. Zhang, Topological insulators and superconductors, Rev. Mod. Phys. **83**, 1057 (2011).

[10] F. Matusalem, M. Marques, L. K. Teles, L. Matthes, J. Furthmüller, and F. Bechstedt, Quantization of spin Hall conductivity in two-dimensional topological insulators versus symmetry and spin-orbit interaction, Phys. Rev. B **100**, 245430 (2019).

[11] L. Matthes, S. Küfner, J. Furthmüller, and F. Bechstedt, Quantization and topological states in the spin Hall conductivity of low-dimensional systems: An *ab initio* study, Phys. Rev. B **93**, 121106(R) (2016).

[12] L. Matthes, S. Küfner, J. Furthmüller, and F. Bechstedt, Intrinsic spin Hall conductivity in one-, two-, and three-dimensional trivial and topological systems, Phys. Rev. B **94**, 085410 (2016).

[13] J. Li, Y. Li, S. Du, Z. Wang, B.-L. Gu, S.-C. Zhang, K. He, W. Duan, and Y. Xu, Intrinsic magnetic topological insulators in van der Waals layered $MnBi_2Te_4$-family materials, Sci. Adv. **5**, eaaw5685 (2019).

[14] M. M. Otrokov, I. P. Rusinov, M. Blanco-Rey, M. Hoffmann, A. Y. Vyazovskaya, S. V. Eremeev, A. Ernst, P. M. Echenique, A. Arnau, and E. V. Chulkov, Unique thickness-dependent properties of the van der Waals interlayer antiferromagnet $MnBi_2Te_4$ films, Phys. Rev. Lett. **122**, 107202 (2019).

[15] D. Zhang, M. Shi, T. Zhu, D. Xing, H. Zhang, and J. Wang, Topological axion states in the magnetic insulator $MnBi_2Te_4$ with the quantized magnetoelectric effect, Phys. Rev. Lett. **122**, 206401 (2019).

[16] Y. Gong, J. Guo, J. Li, K. Zhu, M. Liao, X. Liu, Q. Zhang, L. Gu, L. Tang, X. Feng *et al.*, Experimental realization of an intrinsic magnetic topological insulator, Chin. Phys. Lett. **36**, 076801 (2019).

[17] Y. Deng, Y. Yu, M. Z. Shi, Z. Guo, Z. Xu, J. Wang, X. H. Chen, and Y. Zhang, Quantum anomalous Hall effect in intrinsic magnetic topological insulator $MnBi_2Te_4$, Science **367**, 895 (2020).

[18] C. Liu, Y. Wang, H. Li, Y. Wu, Y. Li, J. Li, K. He, Y. Xu, J. Zhang, and Y. Wang, Robust axion insulator and Chern insulator phases in a two-dimensional antiferromagnetic topological insulator, Nat. Mater. **19**, 522 (2020).

[19] J. Ge, Y. Liu, J. Li, H. Li, T. Luo, Y. Wu, Y. Xu, and J. Wang, High-Chern-number and high-temperature quantum Hall effect without Landau levels, Natl. Sci. Rev. **7**, 1280 (2020).

[20] Y. Bai, Y. Li, J. Luan, R. Liu, W. Song, Y. Chen, P.-F. Ji, Q. Zhang, F. Meng, B. Tong *et al.*, Quantized anomalous Hall resistivity achieved in molecular beam epitaxy-grown $MnBi_2Te_4$ thin films, Natl. Sci. Rev. **11**, nwad189 (2024).

[21] Z. Li, J. Li, K. He, X. Wan, W. Duan, and Y. Xu, Tunable interlayer magnetism and band topology in van der Waals heterostructures of $MnBi_2Te_4$-family materials, Phys. Rev. B **102**, 081107(R) (2020).

[22] A. Kobiałka, M. Sternik, and A. Ptok, Dynamical properties of the magnetic topological insulator $T\,Bi_2Te_4$ ($T = \mathrm{Mn, Fe}$): Phonons dispersion, Raman active modes, and chiral phonons study, Phys. Rev. B **105**, 214304 (2022).

[23] J. Zhang, D. Wang, M. Shi, T. Zhu, H. Zhang, and J. Wang, Large dynamical axion field in topological antiferromagnetic insulator $Mn_2Bi_2Te_5$, Chin. Phys. Lett. **37**, 077304 (2020).

[24] X.-Y. Tang, Z. Li, F. Xue, P. Ji, Z. Zhang, X. Feng, Y. Xu, Q. Wu, and K. He, Intrinsic and tunable quantum anomalous Hall effect and magnetic topological phases in $XYBi_2Te_5$, Phys. Rev. B **108**, 075117 (2023).

[25] Z. Xu, W. Duan, and Y. Xu, Controllable chirality and band gap of quantum anomalous Hall insulators, Nano Lett. **23**, 305 (2023).

[26] J.-Y. You, Z. Zhang, B. Gu, and G. Su, Two-dimensional room-temperature ferromagnetic semiconductors with quantum anomalous Hall effect, Phys. Rev. Appl. **12**, 024063 (2019).

[27] X. Li, X. Xu, H. Zhou, H. Jia, E. Wang, H. Fu, J.-T. Sun, and S. Meng, Tunable topological states in stacked Chern insulator bilayers, Nano Lett. **23**, 2839 (2023).

[28] Y. Li, J. Li, Y. Li, M. Ye, F. Zheng, Z. Zhang, J. Fu, W. Duan, and Y. Xu, High-temperature quantum anomalous Hall insulators in lithium-decorated iron-based superconductor materials, Phys. Rev. Lett. **125**, 086401 (2020).

[29] Z. Li, Y. Han, and Z. Qiao, Chern number tunable quantum anomalous Hall effect in monolayer transitional metal oxides via manipulating magnetization orientation, Phys. Rev. Lett. **129**, 036801 (2022).

[30] F. Xue, Y. Hou, Z. Wang, Z. Xu, K. He, R. Wu, Y. Xu, and W. Duan, Tunable quantum anomalous Hall effects in ferromagnetic van der Waals heterostructures, Natl. Sci. Rev. **11**, nwad151 (2024).

[31] C. Niu, N. Mao, X. Hu, B. Huang, and Y. Dai, Quantum anomalous Hall effect and gate-controllable topological phase transition in layered $EuCd_2As_2$, Phys. Rev. B **99**, 235119 (2019).

[32] X. Wu, R. Li, X. Zou, B. Huang, Y. Dai, and C. Niu, Robust quantum anomalous Hall effect with tunable magnetization directions and Chern numbers, Phys. Rev. B **108**, 115438 (2023).

[33] H. Pan, Z. Li, C.-C. Liu, G. Zhu, Z. Qiao, and Y. Yao, Valley-polarized quantum anomalous Hall effect in silicene, Phys. Rev. Lett. **112**, 106802 (2014).

[34] H. Pan, X. Li, H. Jiang, Y. Yao, and S. A. Yang, Valley-polarized quantum anomalous Hall phase and disorder-induced valley-filtered chiral edge channels, Phys. Rev. B **91**, 045404 (2015).

[35] J. Zhang, B. Zhao, Y. Yao, and Z. Yang, Robust quantum anomalous Hall effect in graphene-based van der Waals heterostructures, Phys. Rev. B **92**, 165418 (2015).

[36] J. Zhang, B. Zhao, T. Zhou, Y. Xue, C. Ma, and Z. Yang, Strong magnetization and Chern insulators in compressed graphene/CrI_3 van der Waals heterostructures, Phys. Rev. B **97**, 085401 (2018).

[37] R. Zou, F. Zhan, B. Zheng, X. Wu, J. Fan, and R. Wang, Intrinsic quantum anomalous Hall phase induced by proximity in the van der Waals heterostructure germanene/$Cr_2Ge_2Te_6$, Phys. Rev. B **101**, 161108(R) (2020).

[38] M. Vila, J. H. Garcia, and S. Roche, Valley-polarized quantum anomalous Hall phase in bilayer graphene with layer-dependent proximity effects, Phys. Rev. B **104**, L161113 (2021).

[39] J. Zhou, Q. Sun, and P. Jena, Valley-polarized quantum anomalous Hall effect in ferrimagnetic honeycomb lattices, Phys. Rev. Lett. **119**, 046403 (2017).

[40] S. Barman, P. Bhakuni, S. Sarkar, J. Bhattacharya, M. Balal, A. Pariari, M. Huecker, R. Batabyal, A. Chakrabarti, and S. R. Barman, Bilayer stanene on a magnetic topological insulator, arXiv:2310.08265.

[41] See Supplemental Material at http://link.aps.org/supplemental/10.1103/PhysRevB.109.235132 for discussions on methods, theoretical analysis of multimechanism quantum anomalous Hall states, various computational parameters, biaxial-strain-induced potential phase evolutions, phonon spectrums, and various multimechanism quantum anonalous Hall states in other related materials with stacking-order-shifts, which includes Refs. [13,21,22,24,25,33,42–53].

[42] G. Kresse and J. Furthmüller, Efficient iterative schemes for *ab initio* total-energy calculations using a plane-wave basis set, Phys. Rev. B **54**, 11169 (1996).

[43] J. P. Perdew, K. Burke, and M. Ernzerhof, Generalized gradient approximation made simple, Phys. Rev. Lett. **77**, 3865 (1996).

[44] S. Grimme, J. Antony, S. Ehrlich, and H. Krieg, A consistent and accurate *ab initio* parametrization of density functional dispersion correction (DFT-D) for the 94 elements H-Pu, J. Chem. Phys. **132**, 154104 (2010).

[45] V. Wang, N. Xu, J.-C. Liu, G. Tang, and W.-T. Geng, VASPKIT: A user-friendly interface facilitating high-throughput computing and analysis using VASP code, Comput. Phys. Commun. **267**, 108033 (2021).

[46] A. Togo and I. Tanaka, First principles phonon calculations in materials science, Scr. Mater. **108**, 1 (2015).

[47] A. A. Mostofi, J. R. Yates, G. Pizzi, Y.-S. Lee, I. Souza, D. Vanderbilt, and N. Marzari, An updated version of WANNIER90: A tool for obtaining maximally-localised Wannier functions, Comput. Phys. Commun. **185**, 2309 (2014).

[48] N. Marzari and D. Vanderbilt, Maximally localized generalized Wannier functions for composite energy bands, Phys. Rev. B **56**, 12847 (1997).

[49] I. Souza, N. Marzari, and D. Vanderbilt, Maximally localized Wannier functions for entangled energy bands, Phys. Rev. B **65**, 035109 (2001).

[50] Q. Wu, S. Zhang, H.-F. Song, M. Troyer, and A. A. Soluyanov, WANNIERTOOLS: An open-source software package for novel topological materials, Comput. Phys. Commun. **224**, 405 (2018).

[51] X.-L. Qi, Y.-S. Wu, and S.-C. Zhang, Topological quantization of the spin Hall effect in two-dimensional paramagnetic semiconductors, Phys. Rev. B **74**, 085308 (2006).

[52] Q. Wang, J. Zhao, W. Wu, Y. Zhou, Q. Li, M. T. Edmonds, and S. A. Yang, Magnetic and electronic properties of bulk and two-dimensional $FeBi_2Te_4$: A first-principles study, Chin. Phys. B **32**, 087506 (2023).

[53] W.-T. Guo, N. Yang, Z. Huang, and J.-M. Zhang, Novel magnetic topological insulator $FeBi_2Te_4$ with controllable topological quantum phase, J. Mater. Chem. C **11**, 12307 (2023).

[54] Y. Xu, B. Yan, H.-J. Zhang, J. Wang, G. Xu, P. Tang, W. Duan, and S.-C. Zhang, Large-gap quantum spin Hall insulators in tin films, Phys. Rev. Lett. **111**, 136804 (2013).

[55] Y. Xu, P. Tang, and S.-C. Zhang, Large-gap quantum spin Hall states in decorated stanene grown on a substrate, Phys. Rev. B **92**, 081112(R) (2015).

[56] F. Zhu, W. Chen, Y. Xu, C. Gao, D. Guan, C. Liu, D. Qian, S.-C. Zhang, and J. Jia, Epitaxial growth of two-dimensional stanene, Nat. Mater. **14**, 1020 (2015).